Article:

WILEY

A material system with integrated fault diagnosis and feedback controlled self-healing

Oluwafemi Sedoten Kuponu[1] | Visakan Kadirkamanathan[1] |
Bishakh Bhattacharya[2] | Simon Alexander Pope[1]

[1]Department of Automatic Control and Systems Engineering, University of Sheffield, Sheffield, UK

[2]Department of Mechanical Engineering, Indian Institute of Technology Kanpur, Kanpur, India

Correspondence
Simon Alexander Pope, Department of Automatic Control and Systems Engineering, University of Sheffield, Mappin Street, Sheffield S1 3JD, UK.
Email: s.a.pope@sheffield.ac.uk

Funding information
UK-India Education and Research Initiative, Grant/Award Number: IND/CONT/E/11-12/202

Summary
Two significant drawbacks of current self-healing materials are that they are: (1) Passive and as such do not guarantee a match between the healing and damage rate; (2) Not monitored during and after healing, so that the performance of the healed material is not known without retrospective offline testing. As a consequence their application is currently limited in some sectors, such as the aerospace sector where high performance needs to be guaranteed within strict guidelines. This article proposes the first active self-healing material that integrates with control and fault diagnosis to provide a system with a desired healing response. A fault diagnosis algorithm using supervised regression is used to estimate the measure of damage. Then based on this estimate, adaptive feedback control is used to ensure a match between the healing response and the damage rate, while taking into account the nonlinear system dynamics and uncertainty. The system is demonstrated in simulation using a self-healing material based on piezoelectricity and electrolysis. This shows the ability of the integrated subsystems to tackle these two significant drawbacks of most current self-healing systems and will benefit applications with strict performance requirements, or systems operating under harsh conditions or that are remotely accessed.

KEYWORDS
adaptive control, fault diagnosis, self-healing material

1 | INTRODUCTION

Scheduled and condition based maintenance are generally carried out with the aim of preventing catastrophic failure, improving reliability and maximizing or extending the remaining useful life of engineering systems. These forms of maintenance are usually achieved using a range of fault detection, isolation and identification techniques, and have greatly benefited many industries. However, this may prove insufficient for some systems experiencing failure, particularly those with little or no access during operation. For example, the fragmentation and the loss of a wing panel of in-flight passenger aircraft caused by human negligence and progressive crack respectively.[1,2] Such systems can benefit from emerging self-healing materials capable of recovering loss of material properties such as hardness, Young's modulus and so forth.

Instances of aircraft fragmentation, building collapse, crane collapse, turbine blade cracks, pipeline leaks caused by incipient faults associated with human negligence, wear and tear, corrosion, fatigue and so forth that raise safety concerns can be minimized or avoided. Self-healing materials cannot generally by used for abrupt faults, apart from certain systems where the abrupt fault does not cause complete physical failure of the host system, such as for electronic circuits.[3] Most current self-healing materials are at technological readiness levels 1 to 3, that is, basic concept to laboratory use, but their development remains promising and has the potential to change the way materials are used.[4] Nonetheless, efforts towards breaking beyond current technological readiness are evident. This includes self-healing composites which have the filling properties and look of conventional dental materials, but with the added ability to self-heal cracks and prevent bio-degradation.[5–10] Similarly, research in the construction industry involves cementitious composite materials which can self-heal cracks and potentially reduce or prevent building collapse.[11–16] Other promising examples of self-healing research can be found in References 17–19.

Self-healing materials are generally classified either as intrinsic or extrinsic. In intrinsic self-healing materials, healing is achieved through chemical reactions such as hydrogen bonding, ionomeric coupling, thermally reversible reactions, molecular diffusion, chain interlocking, piezo-electrolysis and so forth.[4] These reactions may require some form of energy for example, heat to begin initiation. An illustration is the elastomer depleted by a fired bullet and mended through reversible reaction initiated by the heat generated from the bullet.[20] Examples of reversible reactions requiring high thermal energy trigger are Deils–Ader (DA) and retro-Deils–Alder (rDA).[4] Generally, intrinsic self-healing can be applied numerous times but has limited applications because of its suitability for small damaged areas and high energy requirement.[21] Extrinsic self-healing usually uses microcapsules or vascular tubes within the material to house the healing agents. In microcapsule based self-healing, the crack causes the microcapsules to rupture, leading to openings for healing agents (such as calcium lactate, rapeseed, fluorescent fluid) to flow into the area of interest.[22–24] The number of embedded microcapsules places limitations on the number of times healing occur. In addition, the healing agents may be used with a catalyst to quicken the healing process. Vasculares in the form of capillaries or hollow tubes store and act as a pathway for healing agents in materials. Unlike the capsule based approach, this architecture allows increased dimensionality and supply of healing agent. This also allows connection with an external source. While integrated sensing is not restricted to vascular based self-healing, vascular based self-healing easily integrates with sensing. The author[25] introduced fiber optic sensors to detect changes in pressure and initiate self-healing. Similarly, a vascular based self-healing design with pressure sensors has been presented.[26] A sensed pressure drop initiates the flow of healing agent from an external source. A comprehensive review on intrinsic and extrinsic self-healing methods can be found in these selected recent literatures.[27–30] Regardless of the healing method used, the primary objective is to restore loss of material properties. The restored materials should have gained mechanical properties necessary to maintain functionality. This introduces a relatively satisfactory performance, but a key guide is to use a healing agent capable of restoring functionality to a level equal or greater than the undamaged material properties.[27] Such self-healing materials should be considered as distinct from other self-healing systems which aim to mitigate the effect from, or reduce the propagation of a fault by effectively re-configuring a system. This is usually achieved through some form of adaption to the existing control employed in the system.[31,32] However, in-reality both or even a combination of both approaches is likely to be required to achieve the aim of mitigating the impact of in-service faults on system performance.

However, current self-healing methods are predominantly passive. That is, the incipient cause of the fault is not considered and there is no controlled mechanism to counteract the onset of damage. This typically leads to a mismatch between healing and damage rate. This was highlighted in a previous publication.[33] As a solution to some of the challenges of passive self-healing, an active self-healing system was proposed. This combined the benefits of self-healing and feedback control to achieve a desired healing response capable of matching the damage rate. An electromechanical material whose self-healing mechanism uses piezoelectricity and electrolysis to drive the deposition of healing agent was used to demonstrate active self-healing. The electromechanical material was chosen because of its integrated sensing and actuation. The active control ensured that a desired healing response was achieved but assumed a known damage rate. However, the damage rate is not necessarily known for a given system, it is also time dependent and a function of the operational system parameters. A fault detection and diagnosis (FDD) system can be used to estimate the damage rate of a material system in practice.

A FDD technique is presented in this article and integrated with active control and self-healing. In this work the approach is applied to a model of a beam to ensure that an estimated damage rate that captures the effect of the fault (crack) is used by the active control system to supply external energy needed to give a suitable healing response. The results lead to a system that can potentially be applied in practice. A beam is chosen as it is generically representative of structures commonly used in industrial applications, such as wind turbine blades, automotive suspension/chassis, and

aircraft wing/fuselage. The purpose of this work is to demonstrate the concept in a relatively generic manner. In principle the approach of integrated FDD and active self-healing can be applied to a wider range of applications, providing that a suitable self-healing material/mechanism exists and the desired system performance can be monitored. For example, FDD could be integrated with self-healing mechanisms appropriate for complex/large sections of fiber-reinforced polymer[26] used in aerospace and automotive applications or those for electrical wiring[3] used in a range of electrical and electronic devices.

The article is organized as follows: Section 2 explains the concept of active self-healing, Section 3 models a cantilever beam and its healing mechanism and Section 4 section integrates the model and control design. Section 5 presents the FDD technique used, Section 6 completes the integration of the control design, plant, healing mechanism and FDD, and the Section 7 presents the simulation results.

2 | ACTIVE SELF-HEALING ARCHITECTURE

Some of the limitations of the typical self-healing process in Figure 1 are: (Can the following four points be an itemised lisas per the original manuscript, otherwise the following text does not make full sense)

1. Healing is initiated after the onset of failure. The detection of a fault prior to failure and the initiation of preemptive healing to prevent failure does not occur.
2. Healing typically occurs in open loop. The process is unable regulate the healing rate to match a desired response, or compensate for uncertainty/disturbance.
3. Healing occurs passively and is usually not directed to the region of failure. This can affect the effectiveness of the healing at the fault location.
4. The healing process and healed system is not monitored, so that the current state of the healing process and recovered system properties are not accurately known.

Despite these limitations, the ability of "passive" self-healing mechanisms to react to and heal a range of fault types, has been investigated quite widely and has the potential to provide improved performance and safety for systems in a range of application domains. This is usually without the need for operator input and external influence or monitoring. However, active self-healing consisting of three integrated subsystems has the potential to tackle some of these limitations. The three subsystems are self-healing system, control system and FDD system; and together, they form a closed loop system shown in Figure 2. In this system the disturbance will include the input which generates the fault in the material. The FDD subsystem monitors the self-healing material using the sensor measurements and through detection, isolation, and identification of a fault, generates an estimate that measures the effect of damage. This allows the onset and propagation
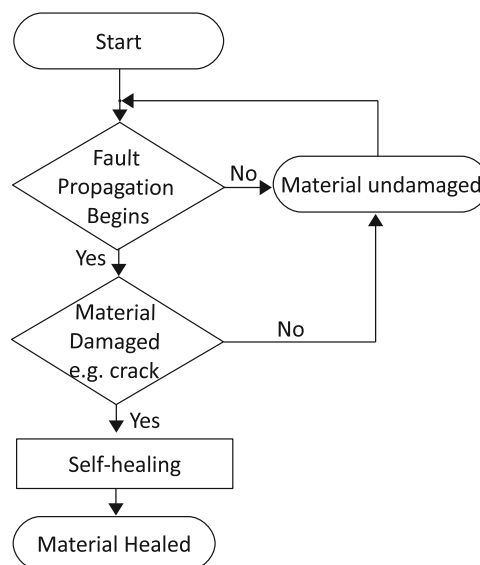

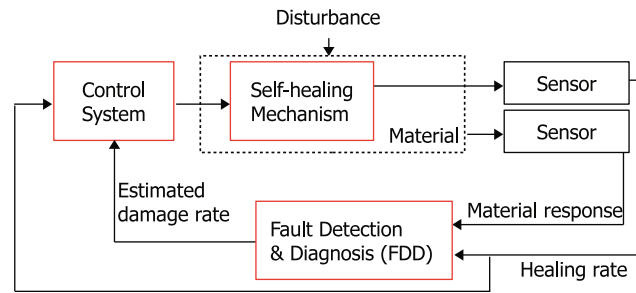**FIGURE 1** A flow chart of a typical passive self-healing process

FIGURE 2   Generic concept of active self-healing integrates control, fault diagnosis, and self-healing.

of a fault to be monitored and self-healing appropriately initialized, with the aim of tackling the first limitation listed above. By continuing to monitor the system during healing the effect of the healing on certain performance criteria can be determined online. This tackles the fourth limitation. The estimated measure of damage produced by the FDD sub-system is matched by the active control subsystem. That is, the control algorithm ensures a desired healing response is achieved by applying an external input to regulate factors such as pH level, temperature, flow rate, release mechanism and so forth affecting the reaction kinetics of a healing process. Recent work has indicated the potential of this approach to tackle the second limitation.[33]

The control subsystem also takes into account system uncertainties and disturbances during healing to ensure that the healing rate matches the estimated damage rate. In the present work a passive self-healing process whose healing mechanism is driven by piezoelectricity and electrolysis[34,35] is adopted to demonstrate the advantages of such an active self-healing system. In this system the disturbance input generates a piezo-induced voltage. However, since electrolysis has an inherent deadzone, the self-healing processes will only activate once the voltage rises above a certain threshold. If the voltage is sufficiently large then the system will operate in a passive mode driven only be the disturbance input, that is, no external control energy is added to the system. Thus for small disturbance inputs a fault can still propagate and even if the disturbance input is sufficiently large to overcome the deadzone, it is unlikely that the resulting healing rate will match the failure rate. The introduction of the control algorithm matches the outcome of the FDD and supplies an external voltage, while taking into account the insufficient passive piezo-induced voltage so as to overcome the inherent deadzone. This ensures that the current flowing during electrolysis produces the desired healing response.

Overall, active self-healing ensures that a healing process is regulated and a proper match between the healing and damage rate is achieved. This has the potential to break beyond current technological readiness levels of most self-healing applications, reduce human negligence and improve reliability of engineering systems.

3 | SYSTEM MODEL

The approach taken is to develop a model of an integrated FDD and active self-healing system that is suitable to demonstrate the general approach without focusing too closely on an application domain. As such the mechanical system is chosen to be an idealized example of a structure commonly found in a range of engineering applications. The self-healing mechanism is chosen for its general ease of use in an active form. Of particular focus is an input variable that can be easily controlled by a control system, without the need for additional actuation which adds further assumptions and model complexity. Inputs to the system are chosen for demonstration purposes and to make the example even more tractable. In principle the general approach can be extended to a wide range of applications, as long as relevant system variables can be measured, an appropriate FDD algorithm developed and a suitable self-healing system integrated into the system and actuated by a controllable voltage input. Addressing a more specific engineering application would potentially hide the generality of the approach and require appropriate example specific issues to be addressed for the work to be applicable.

3.1 | Mechanical structure

The chosen structure is an idealized cantilever beam, which is an approximation to structures typically used in a wide range of industrial systems, such as footbridges, wind turbine blades, cranes, balconies, airliner wings and so forth. For
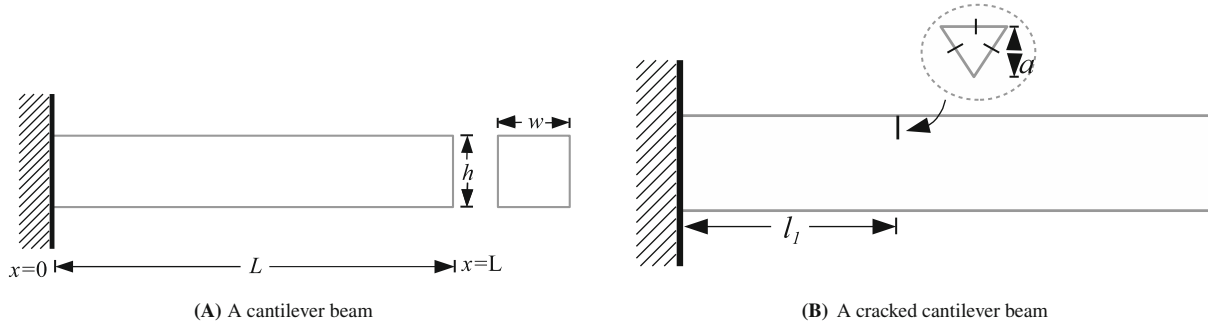
design and analysis, Figure 3A shows a healthy cantilever beam of length L, width w and depth h. Euler–Bernoulli beam theory is used to model the beam.[36]

The free vibration of a beam with density ρ, Young's modulus E, cross sectional area A and second moment of inertia I is expressed in (1):

$$EI\frac{\partial^4 y(x,t)}{\partial x^4} + \rho A\frac{\partial^2 y(x,t)}{\partial t^2} = 0, \tag{1}$$

where $y(x,t) = \sum_{n=1}^{\infty} Y_n(x)\sin(\omega_n t)$ is the displacement at location x due to the mode shapes Y_n with natural frequencies ω_n (rad/seconds).

Following from (1), an intact and undamped beam's mode shapes Y_n is given by (2), where $\lambda_n = \sqrt[4]{\omega_n^2 \rho A L^4/EI}$.[36]

$$Y_n(x) = \eta_1 \cosh\left(\lambda_n\frac{x}{L}\right) + \eta_2 \sinh\left(\lambda_n\frac{x}{L}\right)$$
$$+ \eta_3 \cos\left(\lambda_n\frac{x}{L}\right) + \eta_4 \sin\left(\lambda_n\frac{x}{L}\right). \tag{2}$$

Following the application of the boundary conditions in Equation (3) at $x = 0$ and $x = L$, the unknowns η_{1-4} in (2) can be determined. This gives (4).

$$Y_n(0) = Y_n'(0) = 0,$$
$$Y_n''(L) = Y_n'''(L) = 0, \tag{3}$$

$$\begin{bmatrix} 1 & 0 & 1 & 0 \\ 0 & 1 & 0 & 1 \\ \cosh(\lambda_n) & \sinh(\lambda_n) & -\cos(\lambda_n) & -\sin(\lambda_n) \\ \sinh(\lambda_n) & \cosh(\lambda_n) & \sin(\lambda_n) & -\cos(\lambda_n) \end{bmatrix} \begin{bmatrix} \eta_1 \\ \eta_2 \\ \eta_3 \\ \eta_4 \end{bmatrix} = 0. \tag{4}$$

If a crack of depth a occurs at l_1 in the beam in Figure 3B, the beam can be divided into two sections. If Y_r and Y_l is the modal deflection on the right and left of the crack respectively, the general equation for the two sections can be written as (5) and (6).

$$Y_{r_n}(x) = \alpha_1 \cosh\left(\lambda_{d_n}\frac{x}{L}\right) + \alpha_2 \sinh\left(\lambda_{d_n}\frac{x}{L}\right)$$
$$+ \alpha_3 \cos\left(\lambda_{d_n}\frac{x}{L}\right) + \alpha_4 \sin\left(\lambda_{d_n}\frac{x}{L}\right), \tag{5}$$

$$Y_{l_n}(x) = \beta_1 \cosh\left(\lambda_{d_n}\frac{x}{L}\right) + \beta_2 \sinh\left(\lambda_{d_n}\frac{x}{L}\right)$$
$$+ \beta_3 \cos\left(\lambda_{d_n}\frac{x}{L}\right) + \beta_4 \sin\left(\lambda_{d_n}\frac{x}{L}\right). \tag{6}$$

(A) A cantilever beam

(B) A cracked cantilever beam

FIGURE 3 Uncracked and cracked cantilever beams. (A) A cantilever beam; (B) a cracked cantilever beam

An additional stiffness Θ given by (7) is used to model the crack.[37] v is the Poisson's ratio.

$$\Theta = \frac{EI}{6(1-v^2)h} \times \frac{1}{J(a,h)}, \tag{7}$$

$$J(a,h) = 1.8224\left(\frac{a}{h}\right)^2 - 3.95\left(\frac{a}{h}\right)^3 + 16.375\left(\frac{a}{h}\right)^4$$
$$- 37.226\left(\frac{a}{h}\right)^5 + 76.81\left(\frac{a}{h}\right)^6 - 126.9\left(\frac{a}{h}\right)^7$$
$$+ 172\left(\frac{a}{h}\right)^8 - 143\left(\frac{a}{h}\right)^9 + 66.56\left(\frac{a}{h}\right)^{10}. \tag{8}$$

The additional boundary conditions introduced by the crack at l_1 are expressed in (9):[37,38]

$$Y_{l_n}(l_1) = Y_{r_n}(l_1)$$
$$Y''_{l_n}(l_1) = Y''_{r_n}(l_1)$$
$$Y'''_{l_n}(l_1) = Y'''_{r_n}(l_1)$$
$$\frac{EI}{\Theta}Y''_{l_n}(l_1) + Y'_{l_n}(l_1) = Y'_{r_n}(l_1). \tag{9}$$

By applying the boundary conditions (9) to (5)–(6), the unknowns α_{1-4} and β_{1-4} can be solved. This gives (10).

$$\begin{bmatrix} AA & BB \end{bmatrix} \begin{bmatrix} \alpha_c \\ \beta_c \end{bmatrix} = 0, \tag{10}$$

$$AA = \begin{bmatrix}
1 & 0 & 1 & 0 \\
0 & 1 & 0 & 1 \\
z_4 & z_3 & z_2 & z_1 \\
z_4 & z_3 & -z_2 & -z_1 \\
z_3 & z_4 & z_1 & -z_2 \\
\hat{E}z_3 + z_4 & \hat{E}z_4 + z_3 & -\hat{E}z_1 - z_2 & \hat{E}z_2 - z_1 \\
0 & 0 & 0 & 0 \\
0 & 0 & 0 & 0
\end{bmatrix}, \tag{11}$$

$$BB = \begin{bmatrix}
0 & 0 & 0 & 0 \\
0 & 0 & 0 & 0 \\
-z_4 & -z_3 & -z_2 & -z_1 \\
-z_4 & -z_3 & z_2 & z_1 \\
-z_3 & -z_4 & -z_1 & z_2 \\
-\hat{E}z_3 & -\hat{E}z_4 & \hat{E}z_1 & -\hat{E}z_2 \\
z_5 & z_6 & -z_7 & -z_8 \\
z_6 & z_5 & z_8 & -z_7
\end{bmatrix}, \tag{12}$$

$$\alpha_c = \begin{bmatrix} \alpha_1 \\ \alpha_2 \\ \alpha_3 \\ \alpha_4 \end{bmatrix} \quad \beta_c = \begin{bmatrix} \beta_1 \\ \beta_2 \\ \beta_3 \\ \beta_4 \end{bmatrix}, \tag{13}$$

where $z_1 = \sin\left(\lambda_{d_n}\frac{l_1}{L}\right)$, $z_2 = \cos\left(\lambda_{d_n}\frac{l_1}{L}\right)$, $z_3 = \sinh\left(\lambda_{d_n}\frac{l_1}{L}\right)$, $z_4 = \cosh\left(\lambda_{d_n}\frac{l_1}{L}\right)$, $z_5 = \cosh(\lambda_{d_n})$, $z_6 = \sinh(\lambda_{d_n})$, $z_7 = \cos(\lambda_{d_n})$, $z_8 = \sin(\lambda_{d_n})$, and $\hat{E} = \frac{\Theta L}{EI\lambda_{d_n}}$.

The objective will be to determine the location and depth of crack, heal it and monitor the response of the healing or healed system. As the objective of the present work is to investigate the concept of integrated fault diagnosis and feedback controlled self-healing and demonstrate its potential in principle, the practical problem has been simplified to make it more tractable. Only a single crack is assumed in the present work and damping is neglected. Future application to practical systems would need to consider factors such as the onset of multiple cracks, different crack geometries and loading conditions.

3.2 | Self-healing mechanism

The modeled self-healing mechanism is based on piezoelectricity and electrolysis.[34,35] Electromechanical materials with the selected healing mechanism can be used for sensing and actuating. Hence, a suitable choice for demonstrating integrated self-healing, control, and fault diagnosis. Mechanical energy applied to an electromechanical material generates electrical energy which in turn drives the transportation of healing agent for example, copper, nickel and so forth to a damaged area through electrolysis. The self-healing model used is based on previous mathematical formulations.[33,39] The voltage V generated when a force $f(t)$ is applied to an electromechanical material can be expressed using a state-space model equations expressed by (14) and (15).

$$\begin{bmatrix} \ddot{x} \\ \dot{x} \\ \dot{V} \end{bmatrix} = \begin{bmatrix} 0 & -\frac{k}{M} & \frac{d_{33}zk}{M} \\ 1 & 0 & 0 \\ -\frac{d_{33}zk}{C} & 0 & -\frac{1}{RC} \end{bmatrix} \begin{bmatrix} \dot{x} \\ x \\ V \end{bmatrix} + \begin{bmatrix} -\frac{1}{M} \\ 0 \\ 0 \end{bmatrix} f(t), \tag{14}$$

$$y = \begin{bmatrix} 0 & 0 & 1 \end{bmatrix} \begin{bmatrix} \dot{x} \\ x \\ V \end{bmatrix}. \tag{15}$$

The terms used in (14) and (15) include the capacitance C, Resistance R, piezoelectric stiffness $k = \frac{E_p A}{h_p}$, relative stack displacement x, number of piezoelectric layers z, piezoelectric Young's modulus E_p, piezoelectric stack height h_p and piezoelectric coupling coefficient d_{33}.

The voltage generated in (15) results in a current flow $\dot{Q}_a$ given in (16) to drive the electrolysis process.

$$\dot{Q}_a(t) = mV(t) + \Delta I(t), \tag{16}$$

$$\Delta I(t) = \begin{cases} -mE_{rev} & \text{for } V(t) > E_{rev}, \\ -mV(t) & \text{for } V(t) \leq E_{rev}, \end{cases} \tag{17}$$

(16) contains the term ΔI used to depict the inherent nonlinearity (deadzone) of an electrolytic process. Sufficient voltage is required to overcome several barriers including the reversible potential of the electrolyte, over-potential of the electrodes and the ohmic and membrane resistance coupled all together as E_{rev}. m is a positive slope and $E_{rev} > 0$.

4 | INTEGRATION OF SYSTEM MODEL WITH CONTROL DESIGN

The purpose of introducing control is to match the damage rate by applying sufficient external energy and to overcome the inherent deadzone in the self-healing mechanism. Adaptive sliding mode control is used as it is known to handle the non-linearity associated with this system. Unlike fixed gain control, adaptive control compensates for system changes by adjusting the control gains at every time instant. Thus, used to control the self-healing system. The adaptive control design is based on a previous formulation.[33,39]

First, the modeled self-healing mechanism (16) is redefined to include the adaptive control output $U(t)$ to give (18). The input voltage to the polymer electrolyte is now the sum of the voltage $V(t)$ created by the piezoelectric effect in

response to the disturbance force and the additional adaptive feedback control voltage $U(t)$.

$$\dot{Q}_a(t) = m(V(t) + U(t)) + \Delta I(t). \tag{18}$$

The design of an adaptive sliding mode controller involves choosing a surface s and designing a controller that ensures that the surface $s = 0$. By driving all the system trajectories to the surface $s = 0$, a proper tracking of the estimated damage rate $\dot{Q}_{ref}$ is guaranteed. The surface s is expressed in (19).

$$s(t) = \lambda_c \tilde{Q}(t), \tag{19}$$

$$\dot{s}(t) = \lambda_c m(V(t) + U(t)) + \lambda_c\left(\Delta I(t) - \dot{Q}_{ref}(t)\right). \tag{20}$$

The term λ_c is strictly positive, $\tilde{Q}(t) = Q_a(t) - Q_{ref}(t)$ and the derivative of the surface s introduces the adaptive control law $U(t)$. The tracking error is $\dot{\tilde{Q}}(t) = \dot{Q}_a(t) - \dot{Q}_{ref}(t)$.

During the control design, the following assumptions hold:

1. The slope m is unknown but bounded, that is, $m \in [m_{min} \; m_{max}]$.
2. The term V is unknown.
3. E_{rev} is also unknown but bounded, that is, $E_{rev} \in [E_{revmin} \; E_{revmax}]$.
4. The term $\Delta I(t)$ is unknown but bounded. That is, $|\Delta I(t)| \leq \rho_c$ and $\rho_c = m_{max}E_{revmax}$.
5. The reference model $\dot{Q}_{ref}$ is known.

Parameters such as V and $\phi = 1/m$ are not known and are estimated as $\hat{V}$ and $\hat{\phi}$ respectively, such that $\tilde{V} = \hat{V} - V$ and $\tilde{\phi} = \hat{\phi} - \phi$. To ensure that the trajectories of the system move to the surface, the control law expressed in (21) satisfies $\frac{1}{2}\frac{d}{dt}s^2 \leq -\eta|s|$. That is, the squared distance of all system trajectories to the surface must be non-increasing. The terms K_d and η are both positive constant.

$$U(t) = -K_d s(t) - V(t) - \frac{1}{m}\left(\Delta I(t) - \dot{Q}_{ref}(t)\right) - \eta sgn(s(t)). \tag{21}$$

The sign function in (21) could have an adverse effect on the control law. This phenomenon is known as chattering and can be eliminated by using a tuning error s_ϵ instead.

$$s_\epsilon = s - \epsilon sat\left(\frac{s}{\epsilon}\right), \tag{22}$$

$$sat(z) = \begin{cases} 1 & \text{for } z \leq 1, \\ z & \text{for } -1 < z < 1, \\ -1 & \text{for } z \leq -1. \end{cases} \tag{23}$$

$\Delta I(t)$ is also unknown but bounded by $\rho_c = m_{max}E_{revmax}$, that is, $\Delta I(t) \leq \rho_c$. Hence, the designed control law is expressed in (24).

$$U(t) = -K_d s(t) - \hat{V} + \hat{\phi}\dot{Q}_{ref}(t) - k^*sat\left(\frac{s}{\epsilon}\right), \tag{24}$$

where $k^* \geq \rho_c/m_{min}$ and $k^*sat(s/\epsilon)$ introduces robustness that compensates for $\Delta I(t)$.

It is essential that the changing adaptive gains $\hat{V}$ and $\hat{\phi}$ in (25) and (26) do not drive the system into instability. This is ensured by evaluating the adaptive gains using Lyapunov stability theory. A comprehensive formulation can be found in References 33,39.

$$\dot{\hat{\phi}} = -\gamma\lambda_c\dot{Q}_{ref}(t)s_\epsilon, \tag{25}$$

$$\dot{\hat{V}} = \lambda_c\Gamma s_\epsilon. \tag{26}$$

5 | FAULT DETECTION AND DIAGNOSIS (FDD)

Previous work has observed that the curvature of a beam is more sensitive to damage than its mode shape.[40–42] As such, the radius of curvature κ expressed in (27) is used for this analysis. $M(x)$ represents the bending moment and the product EI the flexural stiffness of the beam. Changes in the curvature are used as an indicator of abnormality, For example, damage at location x which introduces a reduced flexural stiffness, increases the curvature. It is noted that there are other approaches which could be used to determine fault location based on changes in flexural stiffness.[31,32]

$$\kappa(x) = \frac{M(x)}{EI}. \tag{27}$$

The radius of curvature (27) can be approximated from the beam deflection at the ith node of q number of elements, using the central difference in (28). l is the element length.

$$Y_i'' = \frac{Y_{i+1} - 2Y_i + Y_{i-1}}{l^2}. \tag{28}$$

This gives an approximate radius of curvature (29), for the nth mode shape.

$$Y_n^{rad} = \begin{bmatrix} Y_{n_2}'' & Y_{n_3}'' & \cdots & \cdots & Y_{n_{q-1}}'' \end{bmatrix}. \tag{29}$$

Y_{rad} in (30) is formed from the curvature of r number of mode shapes.

$$Y_{rad} = \begin{bmatrix} Y_1^{rad} \\ \vdots \\ Y_r^{rad} \end{bmatrix}_{r \times (q-2)} \tag{30}$$

A proper orthogonal decomposition (POD) is used to extract the features that will be used for detection and diagnosis. It is employed to separate components that do not change in the signal Y_{rad} in (30), from those that do. Y_{rad} is optimally approximated as the sum of linear weightings expressed in (31).[43,44] φ_k are the POD mode (spatial basis function). They are fixed and must be orthonormal (32) and satisfy (33). The amplitude c_k changes and is the signal used for detection and diagnosis.

$$Y_{rad} \approx \sum_{k=1}^{r} c_k \varphi_k, \tag{31}$$

$$\int \varphi_i \varphi_j dx == \begin{cases} 1 & \text{for } i = j, \\ 0 & \text{for } i \neq j, \end{cases} \tag{32}$$

$$\min \left(\left\| Y_{rad} - \sum_{k=1}^{r} c_k \varphi_k \right\|^2 \right). \tag{33}$$

The POD is determined in the following manner:

1. Calculate the correlation matrix $C = Y_{rad} Y_{rad}^T$.
2. Calculate the spatial basis functions as the eigenvectors of the eigenvalue problem $C\varphi_k = \lambda_k \varphi_k$.
3. Use the spatial basis functions φ_k to calculate the amplitudes $c_k = \varphi_k^T Y_{rad}$.

The amplitudes c_k are evaluated for both undamaged (c^u) and damaged (c^d) systems, based on the undamaged signal (Y_{rad}^u) and damaged signal (Y_{rad}^d). The amplitude for the undamaged system c^u remains fixed, while the amplitude c^d for the damaged system changes as the fault evolves. The amplitudes can be calculated in real time and the current state of the system is evaluated using the monitoring index given in (34) and (35). δ is the limited used to indicate the detection

of a damaged system and is determined by investigation.

$$\tau(t) = \left| ||c^u|| - ||c^d(t)|| \right|, \tag{34}$$

$$index(t) = \begin{cases} 0, & \text{if } \tau \leq \delta \text{ (no fault)}, \\ 1, & \text{otherwise (fault detected)}. \end{cases} \tag{35}$$

The location l_{est} and depth a_{est} of the crack as it changes over time is determined using the error $E(x, t)$ defined in (36)

$$E(x, t) = |c^u(x) - c^d(x, t)|. \tag{36}$$

Using the expression in (37), the error signal $E(x, t)$ is transformed into its equivalent wavelet function W_f. Wavelet analysis has been shown to be a useful tool which can be used to detect small cracks.[45] This makes it suitable for this analysis of small cracks and cracks which are healing and have a decreasing depth.

$$W_f(s, b) = \frac{1}{\sqrt{s}} \int_{-\infty}^{+\infty} E(x) \Psi^* \left(\frac{x - b}{s} \right) dx. \tag{37}$$

The wavelet transform W_f requires a mother wavelet Ψ. In this case, a Morlet wavelet selected from literature is used.[46] The transformation W_f is a function of the scale parameter s and the translation parameter b, which relate to the scale and location of the crack. The Hölder exponent defines a signal $f(x)$ approximated by a polynomial $Z(x)$ at a local point x_0, such that the coefficient N and Hölder exponent α exist (38). This is used to examine changes in signal by operating on the modulus maxima of the wavelet transform in (37) and is expressed in (39).[47–50]

$$|f(x) - Z(x)| \leq N|x - x_0|^\alpha, \tag{38}$$

$$|W_f(s, b)| \leq N s^\alpha. \tag{39}$$

The plot of the logarithm of (39) can be used to determine the coefficients N and α. Since the crack depth at a given location does not affect the Hölder exponent α, the coefficient N can be used as a measure of the depth of a crack at that location. The measure $\frac{N}{l_{est}^p}$ (p is a positive term) can be introduced to represent the normalized crack depth at a given location. While this formulation gives a measure of how deep a crack is at a given location, its actual depth is unknown.

The actual crack depth is estimated using a supervised regression algorithm (40). The weights ζ, are obtained from prior knowledge of crack depths at relevant given locations.

$$\frac{a_{est}}{l_{est}^p} = [X_c][\zeta]^T, \tag{40}$$

$$X_c = \begin{bmatrix} x_c & x_c^2 & \cdots & \cdots & x_c^r \end{bmatrix}_{1 \times rj}, \tag{41}$$

$$\left(\frac{N}{l_{est}^p} \right)_{normalized} = \frac{\frac{N}{l_{est}^p} - \min \left(\frac{N}{l_{est}^p} \right)}{\max \left(\frac{N}{l_{est}^p} \right) - \min \left(\frac{N}{l_{est}^p} \right)}, \tag{42}$$

$$x_c = \begin{bmatrix} \left(\frac{N}{l_{est}^p} \right)_{normalized} & l_{est} & \Delta f \end{bmatrix}_{1 \times j}, \tag{43}$$

$$\Delta f = \begin{bmatrix} f_{u_1} - f_{d_1} \\ \vdots \\ f_{u_n} - f_{d_n} \end{bmatrix}^T_{1 \times n} \tag{44}$$

$$\zeta = \begin{bmatrix} \zeta_1 & \zeta_2 & \cdots & \cdots & \zeta_{rj} \end{bmatrix}_{1 \times rj}. \tag{45}$$

k-fold cross validation[51] is used to determine r, the polynomial order used to estimate the crack depth. x_c^r is the r times element wise multiplication of x_c. x_c in (43) is determined from (42) and Δf is the deviation in the modal frequencies at a given crack location. The frequency for any ith mode of the intact beam is f_{u_i}, while f_{d_i} is the frequency of a cracked beam. The frequencies are defined for n modes, with $j = 2 + n$. For the purpose of this research, the minimum and maximum values of $\frac{N}{l_{est}^P}$ are defined over all values in the range from 1 to 3 mm.

6 | INTEGRATION OF SYSTEM MODEL AND CONTROL WITH FDD

The integrated model is based on previous experimental work[35] on adaptive polymer composites. In that work two bars constructed of a laminate of a PVDF-HFP piezoelectric polymer electrolyte and carbon-fiber were bolted together using a zinc-coated steel bolt. Under a sustained tensile load the polymer electrolyte deposited copper near the conductive bolt. Tests showed that this increased both the material hardness near the bolt and the tensile load carrying capacity of the bolted laminate bars. This design is modified and several assumptions are made for the purposes of this work. Figure 4 shows a cantilever beam consisting of two sections of carbon-fiber/PVDF-HFP composite connected together with four zinc-coated steel bolts. In contrast to the previous work we consider out-off plane bending of the beam, but the work is readily extendable to in-plane tensile loading. We also consider a sinusoidal external load, which is more relevant to normal operating considerations for a wide-range of engineering applications, when compared to a sustained fixed load. The fault considered is a cut on the surface of the bolt, or in the immediately adjacent laminate. This is analyzed by the proposed fault diagnosis from Section 5 to estimate the crack depth and location. For the purposes of this work the fault is considered as on-setting suddenly, but such that the system does not exhibit total system failure. The method is also applicable to faults which gradually onset and in such a case might also be used to minimize the propagation of the fault.

The voltage demand from the control system activates the required electrodes, which for this system are the bolts across the beam. Each of the r_o electrodes which have individual locations b_{io} ($io \in [1 \ r_o]$), has an activation status (0 for not active and 1 for active), so that s_{act} in (46) defines the location and activation status of the full set of electrodes:

$$s_{act} = \begin{bmatrix} b_1 & b_2 & b_3 & ... & b_{r_o} \\ 0 & 0 & 0 & ... & 0 \end{bmatrix}_{2 \times r_o} \tag{46}$$

Which electrodes need activating is determined from the estimated fault location l_{est}. That is:

$$s_{act}(2, io) = \begin{cases} 1 & \text{if } l_{est} = b_{io}, \\ 0 & \text{otherwise.} \end{cases} \tag{47}$$

The estimated crack depth is then used as an input to a reference model, which is used to calculate the control input, with the objective to match the healing and damage rate. The reference model is expressed in (48) with a gain g and $\frac{a_{est}}{h} \sim [0, 1]$ is the term that captures the crack. No crack is indicated by $\frac{a_{est}}{h} = 0$ and the maximum crack depth by $\frac{a_{est}}{h} = 1$.

$$\dot{Q}_{ref}(t) = g \frac{a_{est}(t)}{h}. \tag{48}$$

The shape formed when a crack occurs is assumed to be an equilateral triangle as shown in Figure 3B. This shape has been chosen simply to demonstrate the concept of active self-healing and may not necessary represent the actual crack
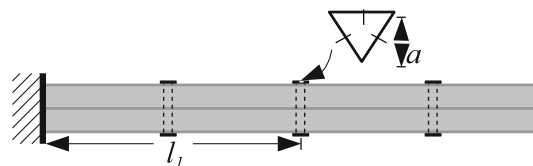

FIGURE 4 A composite cantilever beam with a crack

shape. (49) is the volume to be filled at the occurrence of a crack.

$$V_{fest} = \frac{\sqrt{3}}{3} a_{est}(t_f)^2 w. \tag{49}$$

The term $a_{est}(t_f)$ is the estimated crack depth at the fault time t_f, w, and h are the cantilever beam width and height respectively. Therefore, the estimated crack volume V_{fest} and the square of the estimated crack depth a_{est}^2 are directly proportional, since the beam width is constant. Similarly, the estimated mass M_{cest} required to fill the crack is defined as (50).

$$M_{cest} = \frac{\sqrt{3}}{3} \rho_{sh} a_{est}(t_f)^2 w. \tag{50}$$

During self-healing it is assumed that the fault is healed in a manner such that it recovers the original macro material properties of interest, which in this case is the mass and stiffness of the bar in the region of the crack. In practice, the self-healing process might not recover the original material properties and might act more to mask the effect of the fault. Previous experimental work has shown that the macro properties of interest are recovered by the self-healing process adopted here.[34,35] However, details on how and to what extent the original macro material properties can be recovered for different host structures, would require further experimental investigation with the potential self-healing processes. Complete recovery of the macro material properties is assumed here, since the actual recovered values are not known and its adoption does not affect the investigation of the general concept, which is the main focus in this work. For simplicity and the purpose of demonstrating the proposed concept, it is also assumed that the healing agent evenly coats the internal surface of the crack, so that the crack shape is retained. The healing agent may not evenly deposit in the crack, so this may not necessarily represent the actual healing process. For example the coating might be more uneven.[34,35] The validity of these assumptions can be determined experimentally and would be associated with the material and chemical dynamics of the healing process, which is not the focus of the current work. They are also dependent on the self-healing processes used. The healing process is thus as follows. From the fault time t_f up to the healed time t_h, a total mass $\int_{t_f}^{t_h} \dot{M}_h(t) dt$ of healing agent with density ρ_{sh}, is deposited, The healed time t_h is considered as the time when the total depth filled $a_{sh}(t_h)$ by the healing agent reaches the estimate of the crack depth $a_{est}(t_f)$ at the onset of the crack. It should be noted that ρ_{sh} (the density of the healing agent), does not necessary need to be the same as ρ (the density of the material to be healed). To achieve $a_{sh}(t_h) = a_{est}(t_f)$, (51) must hold. The fault monitoring index in (35) is redefined as (52) during self-healing. The second row of (46) is also reset to zero.

$$\int_{t_f}^{t_h} \dot{M}_h(t) dt = M_{c_{est}}, \tag{51}$$

$$index(t) = \begin{cases} 0, & \text{if } \int_{t_f}^{t_h} \dot{M}_h(t) dt = M_{c_{est}} \text{ (fault healed)}, \\ 1, & \text{otherwise (fault mode).} \end{cases} \tag{52}$$

7 | SIMULATION RESULTS

A carbon-fiber/PVDF-HFP laminate composite beam is used as the basis for the model of the self-healing system. The beam has a clamped boundary condition at one end, creating a cantilever arrangement. It has dimensions 820 mm × 20 mm × 10 mm and is modeled using 25 elements. This makes the cross-section and spacing between the bolts comparable to the previous experimental work.[35] Table 1 gives the parameters of the carbon-fiber/PVDF-HFP laminate composite that are used for the model. Other system and control parameters include $m = 0.1291, E_{rev} = 9.3 \ mV, K^* = 2.5, \lambda_c = 5, K_d = 50, \gamma = 0.5, m_{min} = 0.01, \epsilon = 0.01, g = 1$ and $\delta = 8.4 \times 10^{-7}$. The copper nanoparticles deposited by the healing process[34,35]) have density $\rho_{sh} = 8950 \ kg/m^3$. The system model and its associated parameters have been selected to allow the conceptual idea of integrated self-healing, control, and fault diagnosis to be demonstrated in simulation. The parameter values for the carbon-fiber/PVDF-HFP composite are chosen to provide load-voltage characteristics similar to those of the previous experimental work.[35] The electrical properties of the PVDF-HFP piezoelectric polymer

TABLE 1 Parameters of the composite self-healing beam.[33,35,52,53]

| Properties	Matrix	Carbon-fiber	PVDF-HFP
Young's modulus E	3.43 GPa	275.6 GPa	44 GPa
Poisson ratio v	0.35	0.2	0.33
Density ρ	1250 kg/m³	1900 kg/m³	1780 kg/m³
Volume fraction	17	45	38
Piezoelectric coupling d_{33}	-	-	−24 pC/N
Number of layers z	-	-	130
Resistance R	-	-	23.4 kΩ/m
Capacitance C	-	-	1.94 μF/m

electrolyte are modeled as a lumped cell between each electrode to reduce model complexity at this stage of the work. Their values are given in terms of unit length of the beam. However, it is noted that a distributed parameter model would give a more accurate representation of the copper deposition within the system and is likely to be adopted in future work. Matlab/Simulink is used to complete all simulations and analysis.

The deflections and radius of curvatures of four modes of the uncracked beam and cracked beam with a 3 mm crack at location 295.2 mm are shown in Figure 5. As expected and when compared to the deflections, the radius of curvatures give an obvious distinction between the uncracked and cracked beam. Table 2 also shows that the frequency of the modes of the cracked cantilever beam change. The distinct features associated with the two beam states is determined by applying the POD algorithm to the curvature. Figure 6A shows that the point of maximum difference between the features extracted by applying the POD to the two beam states, indicates the correct location of the crack.

Using the cross-validation shown in Figure 6B, the polynomial order in (40) is selected as $r = 10$. This minimizes the chances of over fitting. The crack diagnosis performance, subject to different depths of crack and associated locations, is shown in Table 2 and Figure 7. A comparison of the proposed fault diagnosis to one using a genetic algorithm, can be found in Appendix A (Table A1).

The response of the open loop passive self-healing system is investigated by introducing a crack of 3 mm at 10 s. The crack is located at 295.2 mm, which corresponds to the location of the second electrode. Forces representative of normal operating characteristics on a full scale structure are introduced. They are harmonic with a frequency of 100 rad/s and a magnitude of 1 and 0.6 N. They are applied at 10 and 150 s respectively and last for the remaining duration of the test. They are representative of forces which occur due to, for example, rotating machinery, footfall, and aerodynamic effects such as turbulence. As a result, the piezoelectric effect of the electromechanical material generates equivalent voltages of 1.86 and 1.11 mV respectively, which are then rectified to drive the electrolytic process. The work assumes perfect rectification at this stage.

Figure 8 shows the results and highlights the inherent drawback of this passive healing process. The piezo-induced voltages are less than E_{rev}. This results in no current flowing to deposit the healing agent, that is, copper nanoparticles (see Figure 8A–C) and as a result no healing occurs. Amplifying the voltages using a gain of 6 results in a current flowing (see Figure 8D,E). This results in an open-loop type response, as opposed to purely passive self-healing. To do this, the piezoelectric and electrolytic components of the self-healing material are considered as separate elements. For this open-loop response, the amplified voltage drops as the crack is healed. When it drops below E_{rev} at 150 s (see black dashes in Figure 8D), the system experiences a dead-zone and the healing stops. Between 10 and 150 s, the chemical kinetic produced deposits a mass. This leads to a reduction in the crack depth (see Figure 8F). However, due to the duration of the applied stress and the inherent dead-zone of the self-healing mechanism, the crack depth does not reduce to zero and as a result the beam is not fully healed. The amplified (open-loop) healing system also does not guarantee a desired healing response. Fundamentally, the issue with this design is that the piezoelectric and electrolyte are mixed as part of the self-healing material and can not be considered as separate elements to allow amplification of the voltage. Nonetheless, the analysis shows the effect of amplification from a conceptual point of view.
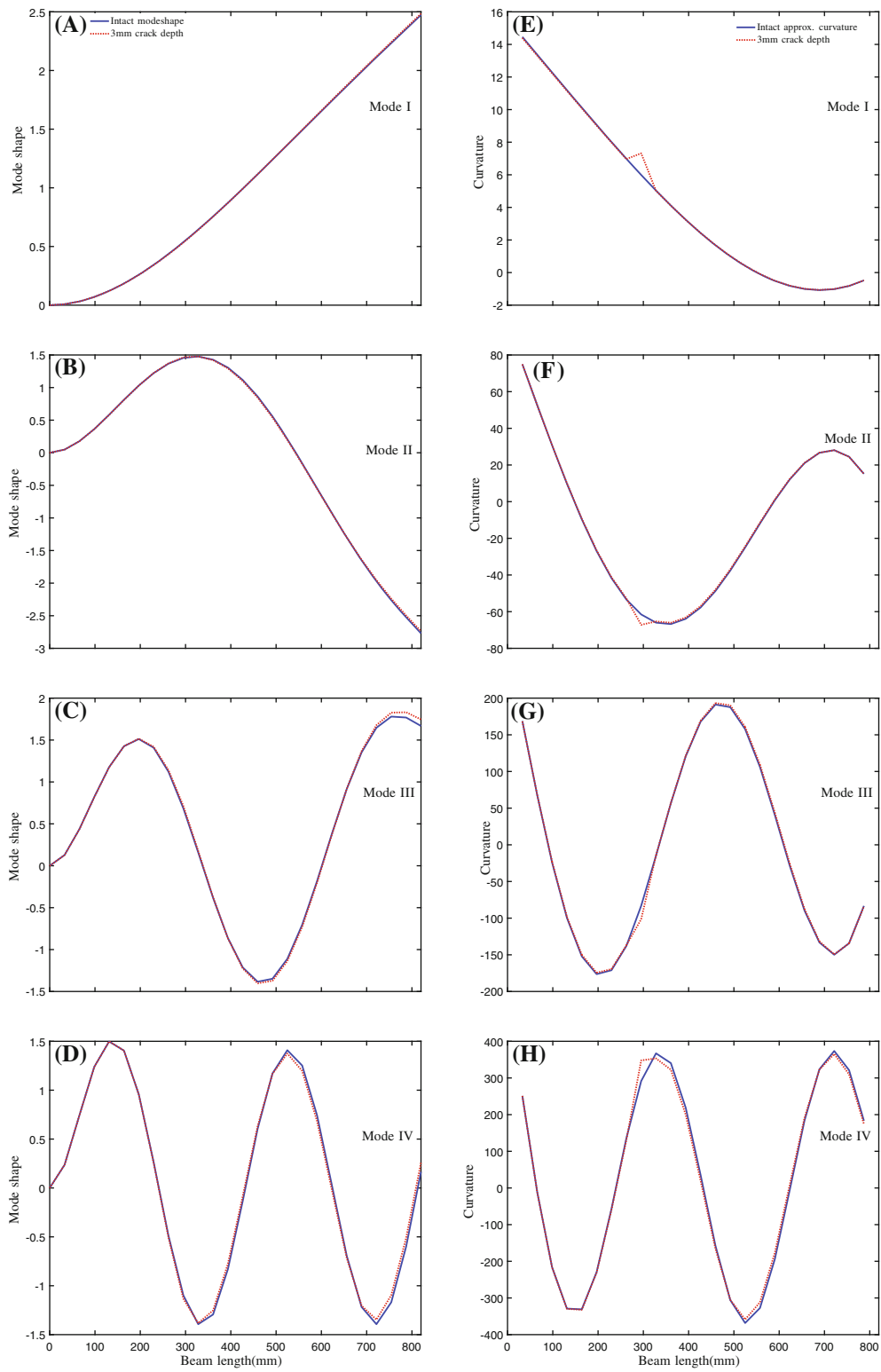
FIGURE 5 Comparison of the mode shape (A–D) and radius of curvature (E–H) of the first four modes of a cantilever beam. The blue line is the undamaged beam and the red line is a beam with a 3 mm deep cracked located at 295.2 mm.

TABLE 2 Results from the FDD for a cracked cantilever beam: Estimate of the crack location and depth and the associated modal frequencies

| Crack location (mm)		Crack depth (mm)			Modal frequency (Hz)			
Actual	**Estimated**	**Actual**	**Estimated**	**% Error**	f_1	f_2	f_3	f_4
-	-	-	-	-	15.51	97.21	272.20	533.40
98.40	98.40	1.00	1.00	0.28	15.49	97.18	272.19	533.34
98.40	98.40	1.50	1.50	0.05	15.46	97.13	272.19	533.28
98.40	98.40	2.00	2.00	−0.24	15.43	97.07	272.18	533.19
98.40	98.40	2.50	2.49	0.22	15.38	97.00	272.17	533.07
98.40	98.40	3.00	2.99	0.48	15.32	96.90	272.16	532.92
196.80	196.80	1.00	1.00	0.04	15.50	97.21	272.03	532.95
196.80	196.80	1.50	1.50	0.00	15.48	97.21	271.83	532.42
196.80	196.80	2.00	2.00	0.04	15.46	97.21	271.55	531.70
196.80	196.80	2.50	2.49	0.21	15.43	97.20	271.19	530.76
196.80	196.80	3.00	3.02	−0.78	15.39	97.20	270.73	529.57
295.20	295.20	1.00	1.00	0.12	15.50	97.16	272.00	533.40
295.20	295.20	1.50	1.50	0.01	15.49	97.11	271.77	533.39
295.20	295.20	2.00	2.00	−0.13	15.48	97.03	271.45	533.39
295.20	295.20	2.50	2.50	−0.04	15.46	96.92	271.03	533.39
295.20	295.20	3.00	2.97	1.11	15.44	96.79	270.50	533.39
393.60	393.60	1.00	1.01	−0.73	15.51	97.11	272.19	532.88
393.60	393.60	1.50	1.50	0.06	15.50	97.00	272.19	532.27
393.60	393.60	2.00	2.00	−0.01	15.50	96.84	272.18	531.44
393.60	393.60	2.50	2.50	−0.01	15.49	96.63	272.17	530.34
393.60	393.60	3.00	3.01	−0.36	15.48	96.37	272.16	528.95
492.00	492.00	1.00	1.01	−0.67	15.51	97.12	272.04	533.29
492.00	492.00	1.50	1.50	0.11	15.51	97.01	271.86	533.16
492.00	492.00	2.00	2.00	0.06	15.51	96.86	271.62	532.99
492.00	492.00	2.50	2.50	0.10	15.50	96.66	271.29	532.76
492.00	492.00	3.00	3.01	−0.47	15.50	96.41	270.88	532.46
590.40	590.40	1.00	1.01	−0.79	15.51	97.17	271.88	533.06
590.40	590.40	1.50	1.50	−0.05	15.51	97.11	271.51	532.68
590.40	590.40	2.00	2.00	0.15	15.51	97.03	271.00	532.15
590.40	590.40	2.50	2.50	−0.00	15.51	96.93	270.32	531.45
590.40	590.40	3.00	2.96	1.17	15.51	96.80	269.46	530.57
688.80	688.80	1.00	0.99	0.85	15.51	97.20	272.08	532.91
688.80	688.80	1.50	1.50	−0.23	15.51	97.19	271.94	532.33
688.80	688.80	2.00	2.00	0.03	15.51	97.18	271.74	531.53
688.80	688.80	2.50	2.50	−0.11	15.51	97.16	271.48	530.48
688.80	688.80	3.00	2.96	1.31	15.51	97.13	271.14	529.11
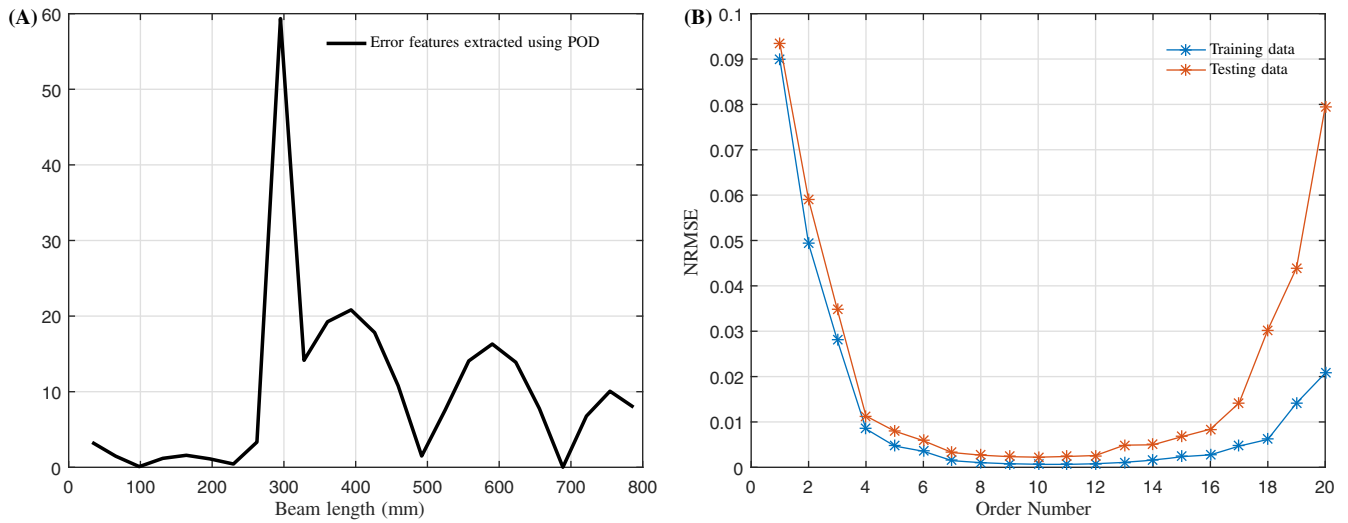
FIGURE 6 (A) Difference between the uncracked and cracked approximate radius of curvature using POD and (36) (B) normalized root mean square (NRMSE) model error plotted against polynomial order
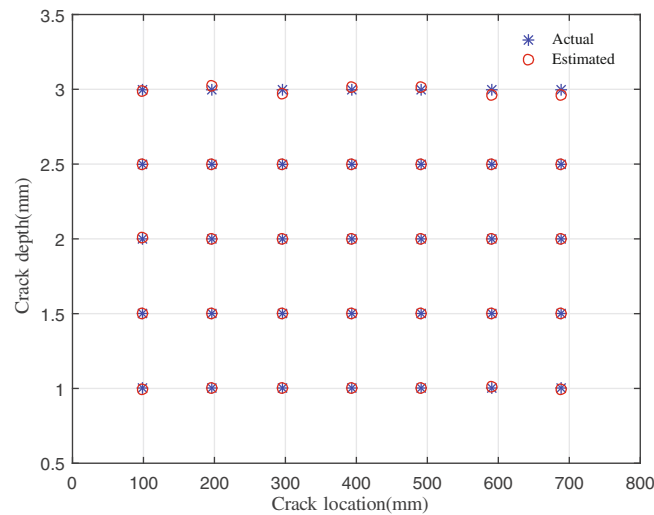

FIGURE 7 Comparison between estimated and actual crack sizes, plotted for different crack depths and locations.

In comparison, Figure 9–11 presents an example of real time monitoring of the self-healing system in the presence of uncertainties or disturbances to demonstrate the concept of unified sensing, diagnosis and active self-healing. In Figure 9 an electrolytic self-healing process is driven by the control input. Initially, a healthy system indicated by the monitoring index indicates (the blue dash-dotted line in Figure 9A). A crack is introduced at 10 s and the system detects it onset (indicated by the blue line in Figure 9A). It estimates its location as 295.2 mm and the control system activates the second electrode based on (46) and (47). The crack depth is estimated as 2.97 mm by the resulting fault diagnosis, a deviation of 1.11% from the actual 3 mm crack depth. An external stimuli (black line of Figure 9B) which aims to minimize the error between the damage and healing rate (see red dashed line and blue line in Figure 9A) is induced by the adaptive controller using the information from the fault diagnosis algorithm. The resulting healing leads to a gradual reduction in the crack depth (see red dotted line in Figure 9C) and the deposited mass tends to the estimated required mass (Figure 9D). However, when the crack depth becomes small, the error in the estimate of its depth increases (see the red dotted line of Figure 9C from about 40 s). The result is that the controller supplies the incorrect voltage to the system (see black line of Figure 9B. This is also seen in in Figure 9A, where the measure of damage and the matching response
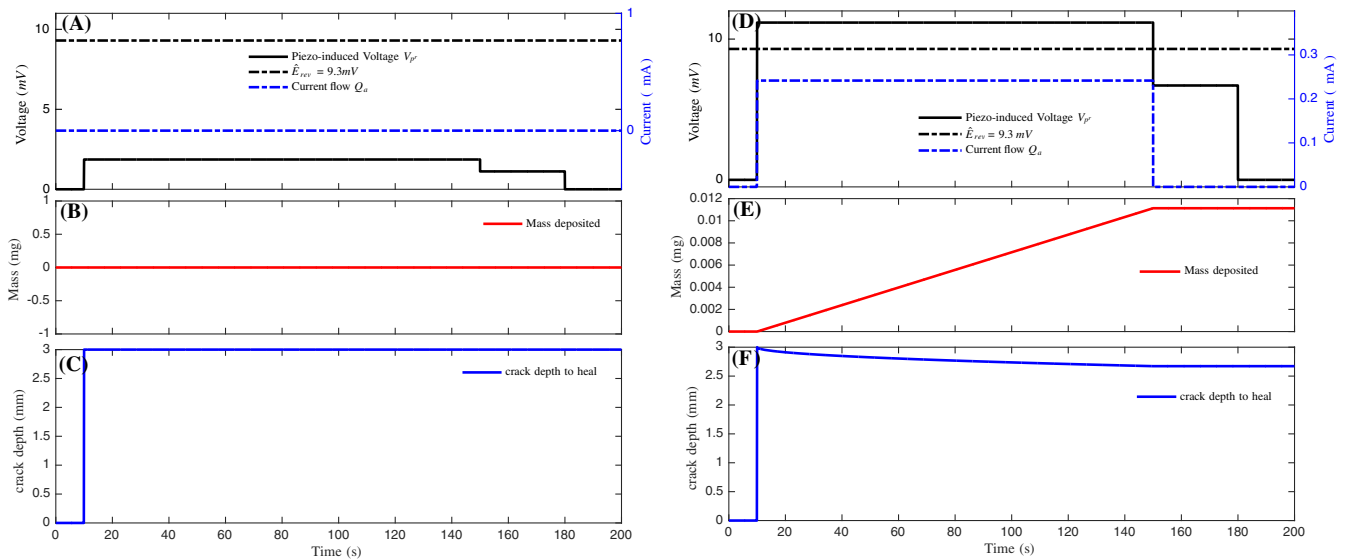
FIGURE 8 Open loop self-healing performance. The fault is a 3 mm deep crack located at 295.2 mm, which onsets at 10 s. Panels (A–C) show how the piezo induced voltage, mass deposited and crack depth change over time. Since the induced voltage is less than E_{rev}, no mass is deposited and as a result no healing occurs. Panels (D–F) show that E_{rev} can be overcome by amplifying the induced voltage, which leads to healing in the form of a reduction in the crack depth.
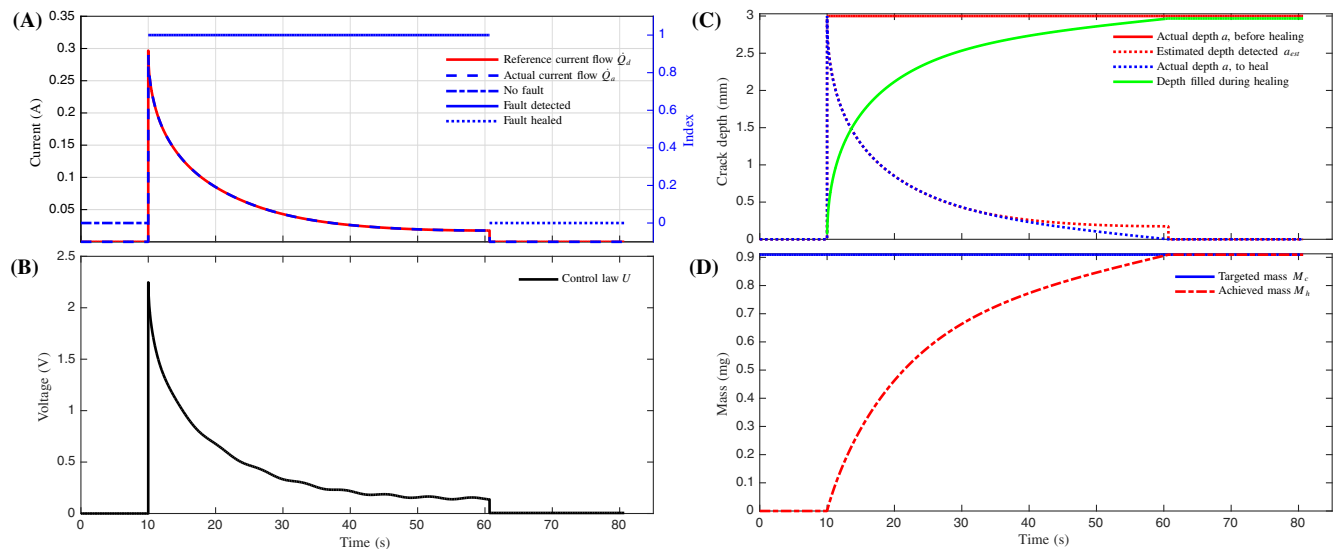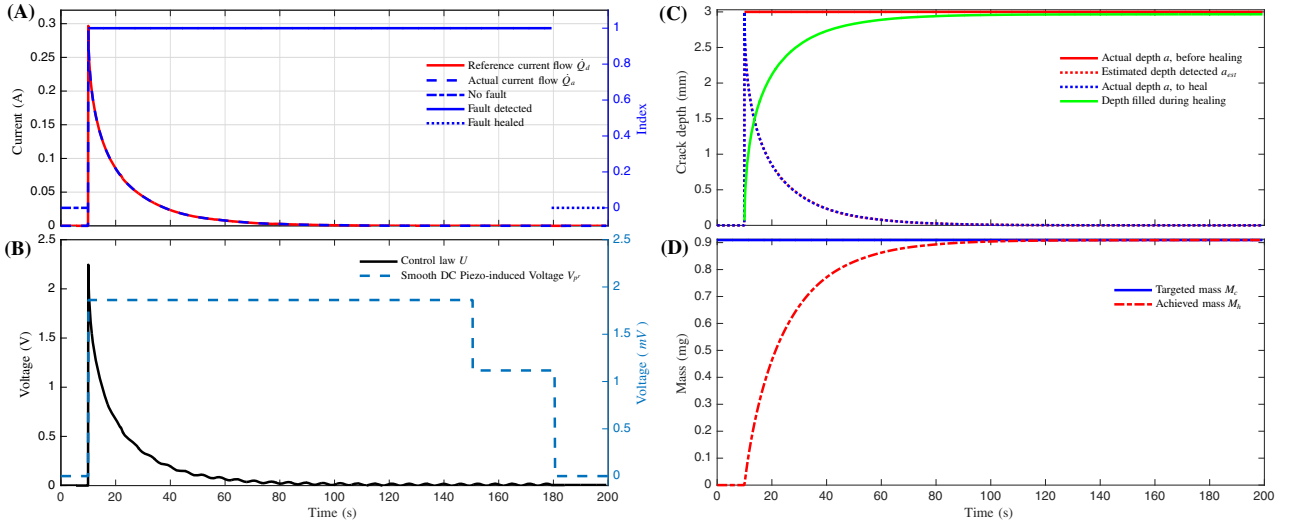

FIGURE 9 Performance of the integrated sensing, diagnostic, and active self-healing system. The fault is a 3 mm deep crack located at 295.2 mm, which onsets at 10 s. In this example the piezoelectric is not included. The electrolytic process is only activated by the feedback control loop, which regulates the voltage to ensure that the crack depth is reduced, that is, the system is healed.

abruptly jump to zero. As a result, the monitoring index indicates that the fault has been healed (blue dotted line in Figure 9A).

The current flow that the control system is able to drive in the electrolysis achieves the required mass estimated by the system. However, its the effectiveness of the feedback controlled self-healing process depends on the accuracy of the fault diagnosis, in-particular the estimate of the smaller crack depths. To improve the estimate of the crack depths down to zero, the weightings Equation (45) are adapted as the crack depth reduces. This is expressed in Equation (53).
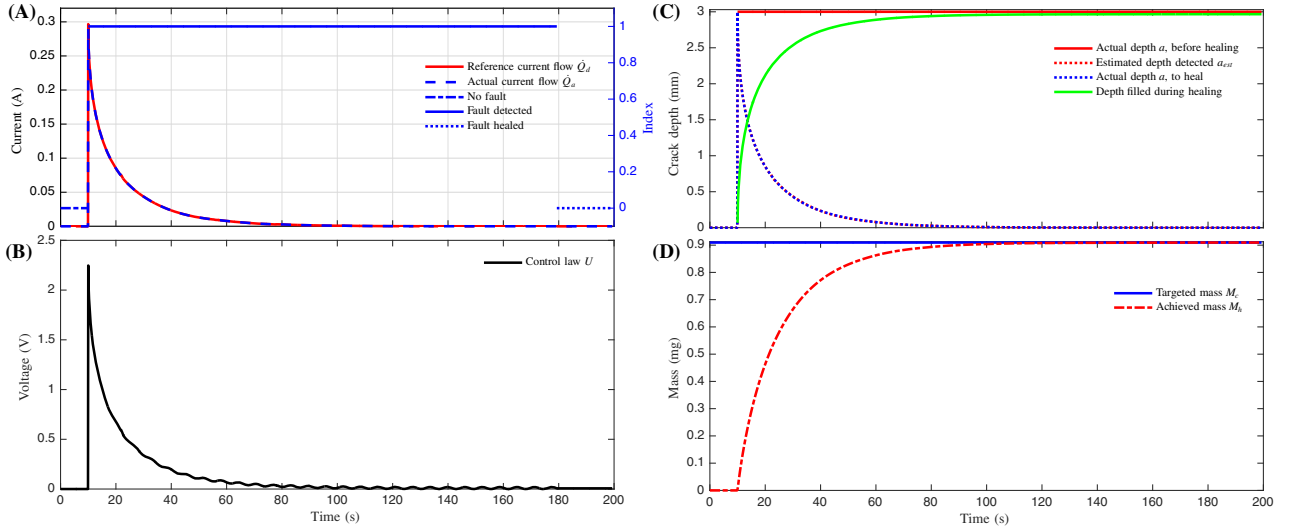
FIGURE 10 Performance of the integrated sensing, diagnostic and active self-healing system with improved performance at lower crack depths. The fault is a 3 mm deep crack located at 295.2 mm, which onsets at 10 s. In this example the piezoelectric is not included

FIGURE 11 Performance of the integrated sensing, diagnostic and active self-healing system when the piezoelectric is included. The piezoelectric contributes to the feedback control voltage used to drive the electrolytic healing process and successfully reduces the depth of the crack. The fault is a 3 mm deep crack located at 295.2 mm, which onsets at 10 s

$$
\zeta = \begin{cases}
\begin{bmatrix} \zeta_{1_i} & \zeta_{2_i} & \cdots & \zeta_{rj_i} \end{bmatrix}_{1 \times rj} & \text{if } a > 0.75 \text{ mm} \\[2ex]
\begin{bmatrix} \zeta_{1_{ii}} & \zeta_{2_{ii}} & \cdots & \zeta_{rj_{ii}} \end{bmatrix}_{1 \times rj} & \text{if } 0.1 < a \le 0.75 \text{ mm} \\[2ex]
\begin{bmatrix} \zeta_{1_{iii}} & \zeta_{2_{iii}} & \cdots & \zeta_{rj_{iii}} \end{bmatrix}_{1 \times rj} & \text{if } 0.03 < a \le 0.1 \text{ mm} \\[2ex]
\begin{bmatrix} \zeta_{1_{iv}} & \zeta_{2_{iv}} & \cdots & \zeta_{rj_{iv}} \end{bmatrix}_{1 \times rj} & \text{if } 0.008 < a \le 0.03 \text{ mm} \\[2ex]
\begin{bmatrix} \zeta_{1_v} & \zeta_{2_v} & \cdots & \zeta_{rj_v} \end{bmatrix}_{1 \times rj} & \text{if } a \le 0.008 \text{ mm}
\end{cases}
\tag{53}
$$
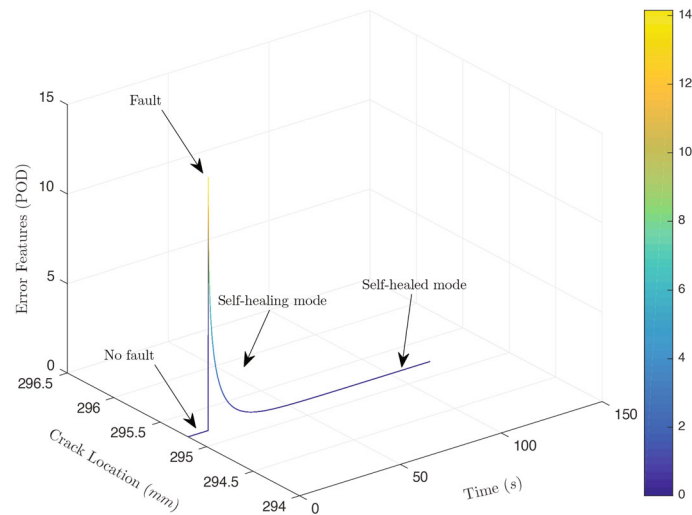
FIGURE 12 The time response of the estimated crack depth shown in terms of the location on the beam. The different time intervals associated with the integrated fault diagnosis and feedback controlled healing system are labeled.

Figure 10 shows the effect of using the adaptive weightings to estimate the crack depth. This results in better estimation of smaller crack depths and as a consequence the external input from the control leads to better healing. Comparing Figure 10 with the equivalent passive and open-loop self-healing in Figure 8D–F, shows that the integrated fault diagnosis and feedback controlled self-healing system achieves a crack depth that is close to zero, while the open-loop self-healing system only reduces the crack depth by less than a quarter of its initial depth. This general trend is observed by running simulations at different crack depths and locations. Figure 11 demonstrates that even in the presence of uncertainties, a composite self-healing material whose healing mechanism is driven by piezoelectricity and adaptive feedback controlled electrolysis, is able to match the estimated damage and healing rate. Figure 12 shows the gradual decrease of the crack depth during the self-healing process. The depth of the crack, which occurs at 10 s, begins to decrease as the healing agent (copper nanoparticles) is deposited.

These simulations demonstrate some of the potential advantages that the unified sensing, diagnosis, and active self-healing system has over equivalent passive or open-loop systems. However, the complexity and cost of the self-healing system is increased by the inclusion of secondary systems, sensors, and actuators. The control system also needs to be correctly designed to ensure stability of the controlled system.

8 | CONCLUSION

To tackle the mismatch between the healing and damage rate common with passive self-healing, the concept of integrated self-healing, control, and fault diagnosis is presented and validated in simulation. A self-healing mechanism that takes advantage of the properties of an electromechanical material to drive mass deposition is considered. A self-healing composite material was modeled as a cantilever beam to represent a range of applications in engineering systems like footbridges, airliner wings, turbine blades and so forth. The system integrates with a developed fault diagnosis and adaptive control system. The proposed fault diagnosis system combines the beam curvature, proportional orthogonal decomposition, wavelet transform, Hölder exponent and supervised regression to estimate the crack depth at different locations. The output of this diagnosis is presented to the adaptive control system as a reference signal. This ensures a match with the diagnosed output for healing. The adaptive control also takes into account the deadzone resulting from insufficient piezo-induced voltage and system uncertainties. Simulations show that the healing and damage rate are effectively matched, as well as showing the effectiveness of the proposed system to changing environments. Simulation results also show the importance of fault diagnosis to accurately estimate the crack depth, particularly at lower depths. Overall, this work has successfully demonstrated that integrated self-healing, control, and fault diagnosis could be pivotal to successful application of self-healing in industrial applications. Active self-healing ensures a proper match that can cancel the effect of damage, improves reliability and can potentially save cost. In this work the FDD and control systems have been chosen based on the dynamics of the operational structure (i.e., cantilever beam) and self-healing mechanism (i.e., piezoelectric

and polymer electrolyte). Other combinations of operational structure and self-healing mechanism will require appropriate FDD and control systems designs to be investigated and implemented. This successfully presented concept requires experimental validation, which will be the focus of future work along with the application of the proposed technique to internal cracks in composite laminates. Future work is likely to require a more empirical based approach to capture real world dynamics of both the fault states of the system and the operation of the self-healing mechanism. Important areas that future work will focus on include the robustness, reliability, and effectiveness of the fault detection and healing in practice. The trade-off between passive self-healing and the added complexity of active self-healing will also need to be investigated and justified in terms of specific applications. Integrated self-healing, control, and fault diagnosis to repair the physical effects of a fault complements alternative work, such as that which re-configures a system to mitigate the effect of a fault and to limit its growth. Future systems might use a combination of both approaches together, with the system re-configuring to maintain performance during operation and to minimize fault propagation, while the approach presented in this manuscript is used to repair the fault.

ORCID
Simon Alexander Pope https://orcid.org/0000-0001-8130-4222

REFERENCES

1. International Aviation Safety Association. China airlines flight CI-611 crash report released; 2005.
2. Smith M, DiGiacomo J. Delta plane loses wing panel during flight CNN.com; 2014.
3. Palleau E, Reece S, Desai SC, Smith ME, Dickey MD. Self-healing stretchable wires for reconfigurable circuit wiring and 3D microfluidics. *Adv Mater*. 2013;25(11):1589-1592. doi:10.1002/adma.201203921
4. Blaiszik BJ, Kramer SLB, Olugebefola SC, Moore JS, Sottos NR, White SR. Self-healing polymers and composites. *Annu Rev Mater Res*. 2010;40(1):179-211.
5. Wu J, Weir MD, Melo Mary Anne S, Xu HHK. Development of novel self-healing and antibacterial dental composite containing calcium phosphate nanoparticles. *J Dent*. 2015;43(3):317-326.
6. Huyang G, Sun J. Clinically applicable self-healing dental resin composites. *MRS Adv*. 2016;1(8):547-552.
7. Wu J, Weir MD, Melo MAS, Strassler HE, Xu HHK. Effects of water-aging on self-healing dental composite containing microcapsules. *J Dent*. 2016;47:86-93.
8. Huyang G, Debertin AE, Sun J. Design and development of self-healing dental composites. *Mater Des*. 2016;94:295-302.
9. Wen Z, Chen J, Wang H, et al. Abalone water-soluble matrix for self-healing biomineralization of tooth defects. *Mater Sci Eng C*. 2016;67:182-187.
10. Wu J, Weir MD, Zhang Q, Zhou C, Melo Mary Anne S, Xu HHK. Novel self-healing dental resin with microcapsules of polymerizable triethylene glycol dimethacrylate and N, N-Dihydroxyethyl-P-toluidine. *Dent Mater*. 2016;32(2):294-304.
11. Sherir MAA, Hossain KMA, Lachemi M. Self-healing and expansion characteristics of cementitious composites with high volume fly ash and MgO-type expansive agent. *Constr Build Mater*. 2016;127:80-92.
12. Wang J, Ersan YC, Boon N, de Belie N. Application of microorganisms in concrete: a promising sustainable strategy to improve concrete durability. *Appl Microbiol Biotechnol*. 2016;100(7):2993-3007.
13. Huang H, Ye G, Qian C, Schlangen E. Self-healing in cementitious materials: materials, methods and service conditions. *Mater Des*. 2016;92:499-511.
14. Mignon A, Devisscher D, Graulus GJ, et al. Combinatory approach of methacrylated alginate and acid monomers for concrete applications. *Carbohydr Polym*. 2017;155:448-455.
15. Mignon A, Vagenende M, Martins J, Dubruel P. Development of amine-based pH-responsive superabsorbent polymers for mortar applications. *Constr Build Mater*. 2017;321:556-564.
16. Ivanov V, Stabnikov V. Advances and future developments of construction biotechnology. In: Construction Biotechnology. In: *Green Energy and Technology*. Singapore: Springer; 2017. doi:10.1007/978-981-10-1445-1_14.
17. Xia NN, Xiong XM, Wang J, Rong MZ, Zhang MQ. A seawater triggered dynamic coordinate bond and its application for underwater self-healing and reclaiming of lipophilic polymer. *Chem Sci*. 2016;7(4):2736-2742.
18. Terryn S, Mathijssen G, Brancart J, Verstraten T, Van Assche G, Vanderborght B. Toward self-healing actuators: a preliminary concept. *IEEE Trans Robot*. 2016;32(3):736-743.
19. Taylor DL. Self-healing hydrogels. *Adv Mater*. 2016;28(41):9060-9093.
20. Frei R, McWilliam R, Derrick B. Self-healing and self-repairing technologies. *Int J Adv Manuf Technol*. 2013;69(5-8):1033-1061.
21. Zhong N, Post W. Self-repair of structural and functional composites with intrinsically self-healing polymer matrices: a review. *Compos A Appl Sci Manuf*. 2015;69:226-239.

22. Zemskov SV, Jonkers HM, Vermolen FJ. A mathematical model for bacterial self-healing of cracks in concrete. *J Intell Mater Syst Struct*. 2012;25(1):4-12.

23. Mirabedini SM, Dutil I, Gauquelin L, Yan N, Farnood RR. Preparation of self-healing acrylic latex coatings using novel oil-filled ethyl cellulose microcapsules. *Progr Org Coat*. 2015;85:168-177.

24. Song YK, Lee KH, Kim DM, Chung CM. A microcapsule-type fluorescent probe for the detection of microcracks in cementitious materials. *Sens Actuat B Chem*. 2016;222:1159-1165.

25. Minakuchi S, Sun D, Takeda N. Hierarchical System for Autonomous Sensing-Healing of Delamination in Large-Scale Composite Structures. *Smart Materials and Structures*. 2014;23(11):115014.

26. Trask RS, Norris CJ, Bond IP. Stimuli-triggered self-healing functionality in advanced fibre-reinforced composites. *J Intell Mater Syst Struct*. 2013;25(1):87-97.

27. Urdl K, Kandelbauer A, Kern W, Müller U, Thebault M, Zikulnig-Rusch E. Self-healing of densely crosslinked thermoset polymers—A critical review. *Prog Org Coat*. 2016;104:232-249.

28. Scheiner M, Dickens TJ, Okoli O. Progress towards self-healing polymers for composite structural applications. *Polymer*. 2016;83:260-282.

29. Hia IL, Vahedi V, Pasbakhsh P. Self-healing polymer composites: prospects, challenges, and applications. *Polym Rev*. 2016;56(2):225-261.

30. Bekas DG, Tsirka K, Baltzis D, Paipetis AS. Self-healing materials: a review of advances in materials, evaluation, characterization and monitoring techniques. *Compos Part B*. 2016;87:92-119.

31. Ashokkumar CR. Active self-healing mechanisms for discrete dynamic structures. *Struct Control Health Monit*. 2013;21:721-740.

32. Ashokkumar CR. Vibration control for structural damage mitigation. *J Vib Control*. 2015;21(15):2995-3006.

33. Kuponu OS, Kadirkamanathan V, Bhattacharya B, Pope SA. Using feedback control to actively regulate the healing rate of a self-healing process subjected to low cycle dynamic stress. *Smart Mater Struct*. 2016;25(5):055028.

34. Soroushian P, Nassar RUD, Balachandra AM. Piezo-driven self-healing by electrochemical phenomena. *J Intell Mater Syst Struct*. 2012;24(4):441-453.

35. Sayayr M, Weerasiri RR, Balachandra AM, Soroushian P. Inherently adaptive polymer nanocomposites. *J Appl Polym Sci*. 2014;131(16):40620.

36. Meirovitch L. *Fundamentals of Vibrations*. International ed. McGraw-Hill; 2001.

37. Vakil-Baghmisheh MT, Peimani M. Crack detection in beam-like structures using genetic algorithms. *Appl Soft Comput*. 2008;8(2):1150-1160.

38. Dong GM, Chen J, Zou J. Parameter identification of a rotor with an open crack. *Eur J Mech-A/Solids*. 2004;23(2):325-333.

39. Kuponu OS, Kadirkamanathan V, Bhattacharya B, Pope SA. Integrated sensing, monitoring and healing of composite systems. *Adv Sci Tech*. 2017;101:62-68.

40. Pandey AK, Biswas M, Samman MM. Damage detection from changes in curvature mode shapes. *J Sound Vib*. 1991;145(2):321-332.

41. Dawari VB, Vesmawala GR. Structural damage identification using modal curvature differences. *IOSR J Mech Civil Eng*. 2013;4:33-38.

42. Wahab MMA, De Roeck G. Damage detection in bridges using modal curvatures: application to a real damage scenario. *J Sound Vib*. 1999;226(2):217-235.

43. Chen H, Reuss DL, Hung DLS. A practical guide for using proper orthogonal decomposition in engine research. *Int J Eng Res*. 2013;14(4):307-319.

44. Buljak V. *Inverse Analyses with Model Reduction: Proper Orthogonal Decomposition in Structural Mechanics*. Springer Science & Business Media; 2011.

45. Yan YJ, Yam LH. Online detection of crack damage in composite plates using embedded piezoelectric actuators/sensors and wavelet analysis. *Compos Struct*. 2002;58(1):29-38.

46. Rao RM. *Wavelet Transforms: Introduction to Theory and Applications*. Pearson Education India; 1998.

47. Angrisani L, Daponte P, D'Apuzzo M. A method for the automatic detection and measurement of transients. Part I: the measurement method. *Measurement*. 1999;25(1):19-30.

48. Douka E, Loutridis S, Trochidis A. Crack identification in beams using wavelet analysis. *Int J Solids Struct*. 2003;40(13):3557-3569.

49. Loutridis S, Douka E, Trochidis A. Crack identification in double-cracked beams using wavelet analysis. *J Sound Vib*. 2004;277(4):1025-1039.

50. Robertson AN, Farrar CR. Singularity detection for structural health monitoring using holder exponents. *Mech Syst Signal Process*. 2003;17(6):1163-1184.

51. Pereira F, Mitchell T, Botvinick M. Machine learning classifiers and fMRI: a tutorial overview. *NeuroImage*. 2009;45(1):S199-S209.

52. Krawczuk M, Ostachowicz W, Zak A. Dynamics of cracked composite material structures. *Comput Mech*. 1997;20(1):79-83.

53. Reverchon E, Cardea S. PVDF-HFP membrane formation by supercritical CO_2 processing: elucidation of formation mechanisms. *Ind Eng Chem Res*. 2006;45(26):8939-8945.

APPENDIX A. COMPARISON OF CRACK DIAGNOSIS ALGORITHM WITH A GENETIC ALGORITHM

TABLE A1 Proposed crack diagnosis applied and compared with genetic algorithm (GE) results obtained in tab. 5 of Reference 37 using the same beam parameters.

Crack location (mm)					Crack depth (mm)				
Actual	Estimated	Error (%)	Estimated (GE)	Error (%) (GE)	Actual	Estimated	Error (%)	Estimated (GE)	Error (%) (GE)
98.4	98.4	0	99.12	0.73	1.0000	1.0005	−0.0516	0.98	−2.00
98.4	98.4	0	97.74	−0.67	2.0000	2.0010	−0.0479	2.01	0.45
98.4	98.4	0	99.93	1.55	3.0000	2.9997	0.0091	2.97	−0.93
196.8	196.8	0	193.8	−1.53	1.0000	1.0026	−0.2606	0.97	−2.60
196.8	196.8	0	194.75	−1.04	2.0000	2.0003	−0.0168	1.99	−0.55
196.8	196.8	0	198.52	0.88	3.0000	3.0042	−0.1413	3.02	0.70
295.2	295.2	0	298.56	1.14	1.0000	0.9998	0.0217	1.02	2.10
295.2	295.2	0	289.79	−1.83	2.0000	1.9999	0.0031	1.98	−1.25
295.2	295.2	0	294.13	−0.36	3.0000	2.9997	0.0092	2.98	−0.77
393.6	393.6	0	400.74	1.81	1.0000	0.9966	0.3397	0.99	−1.20
393.6	393.6	0	394.99	0.35	2.0000	1.9998	0.0091	1.99	−0.45
393.6	393.6	0	395.08	0.38	3.0000	2.9999	0.0021	2.99	−0.50
492.0	492.0	0	489.62	−0.48	1.0000	0.9978	0.2174	0.99	−0.70
492.0	492.0	0	492.16	0.03	2.0000	2.0012	−0.0605	1.97	−1.55
492.0	492.0	0	492.41	0.08	3.0000	3.0006	−0.0197	2.98	−0.53
590.4	590.4	0	589.42	−0.17	1.0000	0.9926	0.7424	0.99	−1.00
590.4	590.4	0	590.48	0.01	2.0000	1.9999	0.0036	2	0.10
590.4	590.4	0	588.1	−0.39	3.0000	3.0000	0.0003	3.02	0.80
688.8	688.8	0	681.99	−0.99	1.0000	0.9957	0.4282	0.98	−1.90
688.8	688.8	0	692.98	0.61	2.0000	1.9995	0.0232	2.04	2.00
688.8	688.8	0	686.83	−0.29	3.0000	3.0004	−0.0129	2.96	−1.27